

SUMMARY REPORT 2017 -2019

Project: PN-III-P4-ID-PCE-2016-0833

Period covered: July 2017 – Dec. 2019

Introduction:

There is an ever-growing demand for data storage capacities in basically all technology and societal fields, with the advent of new concepts such as Data Centers, Cloud Computing and Internet-of-Things that shows steady growth of about 40% per year. Magnetic storage has shown tremendous development in area density and speed, over the last 50 years, however the current hard disk storage is a mature, quite limited, technology with only incremental enhancements possible. As such, a radically new technology will soon be required to keep up with the demand. There are two major breakthroughs that have the potential to allow improvement of the read-write process (speed and power). The first one is represented by our results, obtained in the frame of this project [1], where we have investigated nanomagnet-logic structures compatible with MTJ elements, made of FePt/Cu/Fe trilayers. By investigating the remanent coupling between the hard and soft magnetic layers, through the non-magnetic spacer layer of Cu, we have shown with good precision, how this coupling angle can be conveniently adjusted with high degree of remanence by shortly applied external magnetic fields, via a mechanism called the interlayer exchange coupling. Considering thus this coupling angle as the information storage vector, we propose that not only two magnetization directions can be stored in a magnetic unit cell (up and down) but several orientations of the magnetization vector, orientations given by the appropriately tuned remanent coupling angle, may be stored and retrieved. We are proposing thus an alternative solution to encode information in magnetic films that goes beyond the conventional way of digital magnetic recording. Extremely important for future applications of this concept, we demonstrate, that the remanent coupling angles can be read out via magneto-optical or magneto-resistance effects. In principle, this approach allows to design novel memory cells for advance data storage devices, where multiple states per unit cell can be generated and recorded. The second breakthrough is represented by the recently reported magnetization reversal by femtosecond laser pulses in thin ferromagnetic Gd/Fe/Co films as well as in many other magnetic materials including rare-earth free transition metal multilayers such as Mn-Fe-Al and Co/Ir and CoNiPt/Ir based heterostructures [S. Mangin et al. Nature Materials 13 (2014) 286–292]. Conceptually it represents a new way to control the magnetic state of a medium, at the highest efficiency and shortest possible time-scale. Magnetization reversal by optical means can be done using the laser in the femtosecond regime. The femtosecond magnetic switching has the capacity of pushing the limit of data transfer rates to terabit-per-second range in magnetic recording, at femtojoule per bit switch energies [T. Li et al. Nature 496 (2013) 69–73]. However, there is still long way to go from the fundamental science to scaling up the technology and there is need for taking steps in order to close the gap towards industrially relevant applications.

Project objectives:

1) the creation of magnetic tunnel junction (MTJ) made of rare earth free magnetic compounds (based on Mn/Ir, Mn/Fe/Pt or Co/Ir) as the base foundation for memories; 2) the demonstration of magnetization reversal by femtosecond laser pulses in the MTJ stack; 3) the validation of the performances by testing of the element of memory demonstrator; 4) the conception of an integration platform made of array of MTJs optically switched.

Scientific results:

Stage 1: Creation of a MTJ multilayer as a basis for memory elements

In its simplest form, a MTJ is a trilayer sandwich consisting of two ferromagnetic layers separated by a ultrathin non-magnetic barrier layer. If a voltage is applied to the top and bottom of this structure, and the barrier layer is sufficiently thin, electrons can flow by quantum tunneling through the barrier layer. For tunneling between two magnetic layers the tunneling current is maximum if the magnetization directions of the two magnetic layers are parallel and minimum if their magnetizations are oriented antiparallel. The phenomenon is called tunneling magneto-resistance and is a consequence of the spin dependent tunneling along (CIP) or across (CPP) the structure. The first step that we undertook in the 1st stage of the project, for the creation of the MTJ multilayer, consisted of the development of a trilayer structure made of polycrystalline Fe(10 nm)/Cu(0.6...6.4 nm)/FePt(30 nm) nanolayers that have been prepared by high vacuum ($p = 3 \cdot 10^{-7}$ mbar) rf-magnetron sputtering in an Ar atmosphere of $p = 1 \cdot 10^{-2}$ mbar. These layer systems were deposited on amorphous Ta seed layer on super polished Si substrates and on top they were finally coated against oxidation by 3 nm of Ta₂O₅. To investigate the coupling and conduction phenomena, depending on the tunable thickness of the non-magnetic layer, the sample has been constructed in such a way as to achieve a continuous variation of the Cu layer thickness along the structure. For this purpose, a wedge-shaped Cu spacer layer (slope: $S_{\max} = 3.3$ nm/cm) has been synthesized. The Fe₅₀Pt₅₀ layer achieved its L1₀-phase structure and became magnetically hard after high vacuum annealing at $T = 800$ K for $t = 15$ min. The polycrystalline character of the FePt was determined via atomic force microscopy and x-ray diffraction measurements. We obtained an in-plane texture of the tetragonal c-axes of the grains with an average grain size of about $L = 20$ nm. The random distribution of the grains c-axes results in no preferred direction of the in-plane magneto-crystalline anisotropy after deposition. Surface quality has been checked by x-ray reflection in grazing incidence geometry, data from which a root-mean-square roughness of about $\sigma = 0.4$ nm for the top magnetic layer has obtained. The surface roughness of all interfaces of the system did not exceed $\sigma = 0.7$ nm.

The magnetic properties of the layer system were characterised by longitudinal MOKE measurements at room temperature. Hysteresis loops of the coupled layer system indicate that the magnetic layers are ferromagnetically coupled over the whole range of Cu thickness because only negative exchange fields were observed.

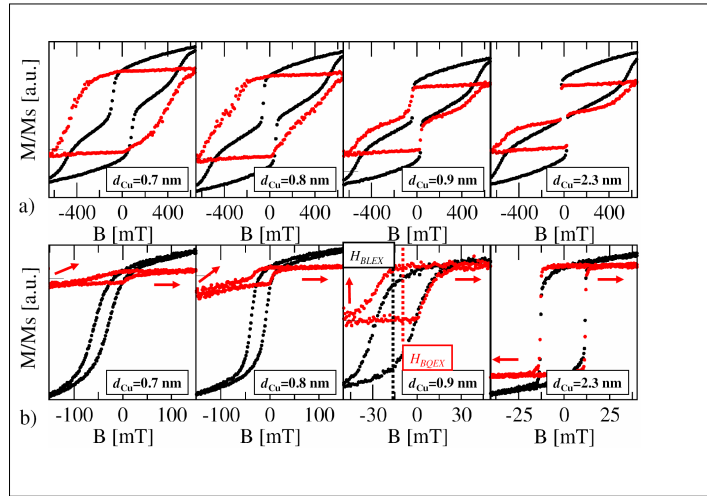


Fig. 1. Room temperature MOKE hysteresis loops for different Cu interlayer thicknesses. The black curves are typical loops - measured with applied fields - the red curves are measurements in remanence mode, where the magnetic fields were temporarily applied for $t = 1$ s. a) major loops and b) easy-axis minor loops, where only the magnetisation direction of the soft magnetic layer is rotating. Additionally, the definition of the bilinear and biquadratic exchange fields (H_{BLEX} , H_{BOEX}) is demonstrated.

In fig. 1 are displayed some examples of the hysteresis loops for different Cu interlayer thicknesses, in particular major (Fig. 2a) and minor (Fig. 2b) loops (B parallel to the FePt easy axis). The black curves are describing typical loops - measured with continuously applied fields - while the red curves are special measurements in remanence mode, where the magnetic fields were temporarily applied for a finite time period $t = 1$ s. In this manner each point of the hysteresis loops was measured in remanence mode. One can see, that for a Cu thickness of about $d_{Cu} = 2.3$ nm the magnetisation of the Fe layer is almost freely adjustable, because the exchange field is negligibly low. For Cu thicknesses less than $d_{Cu} = 2.3$ nm, bi-quadratic coupling is induced and thus different coupling angles are obtained, depending on the magnetic field magnitude and the thickness of Cu. This behaviour is displayed in fig. 2b) with the help of the red arrows inside the minor loop graphics that show the Fe layer magnetisation direction. These different coupling angles may be detected and can be an alternative solution to encode information in magnetic films, in scenarios where multiple states per unit cell (not only “up” and “down”) can be generated and recorded. Such result in spin manipulation and magnetization detection that refers to the observation of the interlayer exchange coupling (IEC) in trilayer systems made of hard and soft magnetic layers, with a metallic non-magnetic layer in between, can be foundational for future applications. We have demonstrated that depending on the layer thickness, the orientation of the magnetic layers can be tuned to either antiparallel or parallel, as required in the MTJ stack. We have also shown that by tuning the IEC we can orient the spin and detect its orientation not only in up and down position, but also in intermediate positions and this opens pathways towards recording multiple bits of information onto the same stack.

The layer stack of the MTJ elements have been determined based on the specific needs of the function to be performed. The systems chosen for the MTJ stack components are derived from Mn-Al and Ir-Mn. Such samples have been deposited by DC - RF sputtering in our dedicated facility at NIMP, a UHV chamber (10^{-8} mbar) with possibility

of simultaneous sputter from 3 targets. Rigorous control of stoichiometry and evaporation rate can be achieved during fabrication. During deposition the base pressure was 3×10^{-6} mbar, used for degassing the samples for 2 hours. The layers were obtained in Ar plasma of low pressure. By applying the rf field the Ar ions are accelerated towards an electrode that contains the metallic target. Ar ions sputter metallic atoms from the target that afterwards are deposited onto the substrate fixed on top of the other electrode (10 cm between electrodes). The working power was ranging between 40 and 180 W, depending on the nature of the metal sputtered. Layered systems with compositions such as [Mn-Ir]/57Fe/Cu/Si and [Mn-Ir]/57Fe/FeNiCr/Si have been prepared and characterized. In order to better quantify the Mn influence on the magnetic and switching behavior of the free magnetic layer in the MTJ stack, several other Mn containing systems have been prepared. A particularly favorable case is represented by the compound $Mn_{55}Al_{45}$ suitable for inclusion in the MTJ stack. For this compound, a structural phase transition has been documented and monitored [A.D. Crisan et al. Mater Charact. 140 (2018) 1-8] during the present project. The ϵ to β -Mn phase transition is particularly favorable for inducing magnetic anisotropy in the case of layer compounds in the MTJ stack. The temperature evolution of the phase composition in the $Mn_{55}Al_{45}$ sample has been followed by using structural temperature-dependent XRD measurements using synchrotron radiation. All the recorded diffractograms were analyzed by a whole-profile fitting procedure in order to retrieve the structural parameters (lattice parameters, relative phase abundance, grain size). As mentioned before, at room temperature, the synchrotron diffractogram of the *as-cast* $Mn_{55}Al_{45}$ alloy have shown mainly a mixture of γ_2 (Al_8Mn_5) (around 75%) and ϵ -phase (around 25%). The ϵ to β -Mn phase transition is initiated at approx. 470°C. The amount of ϵ phase gradually decreases and the ϵ phase disappears above 520°C. The diffraction peaks of the β -Mn phase become visible above this temperature, and the amount of β -Mn increases to reach about 25% at 700°C the maximum temperature attained in this study. The amount of the γ_2 (Al_8Mn_5) phase is constant throughout the *in-situ* temperature-resolved diffraction experiment, although its relative fraction changes, due to the variation of the total scattered X-ray intensity caused by the decomposition of the ϵ phase and the subsequent formation of the β -Mn phase. After constant-rate heating to 700°C, followed by isothermal treatment at this temperature for about 20 min and cooling down to ambient temperature, the specimen consists of a mixture of 75% γ_2 (Al_8Mn_5) phase and β -Mn phase, respectively (Fig. 2).

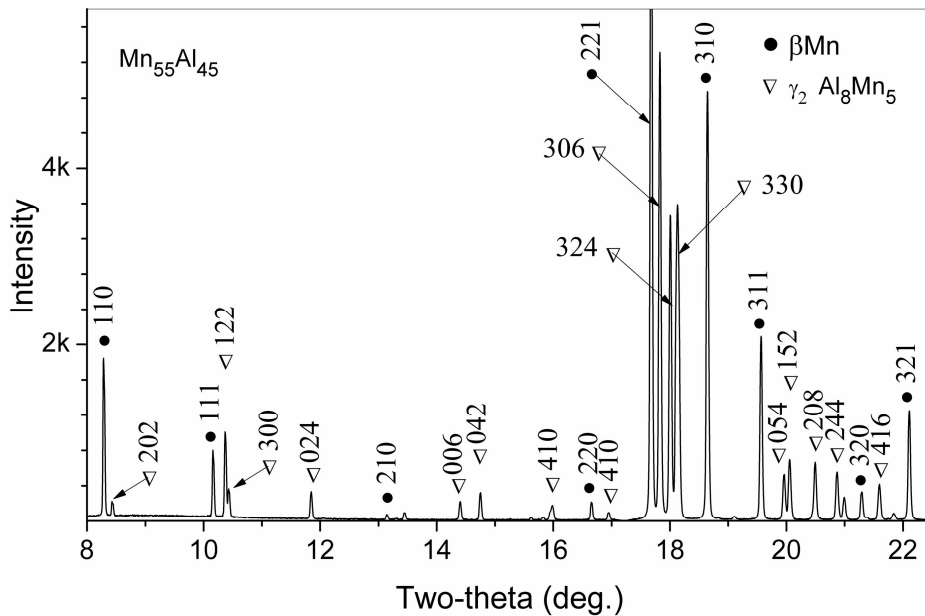


Fig. 2 Indexing of the room temperature XRD pattern of $Mn_{55}Al_{45}$ after heating, isothermal treatment and subsequent cooling.

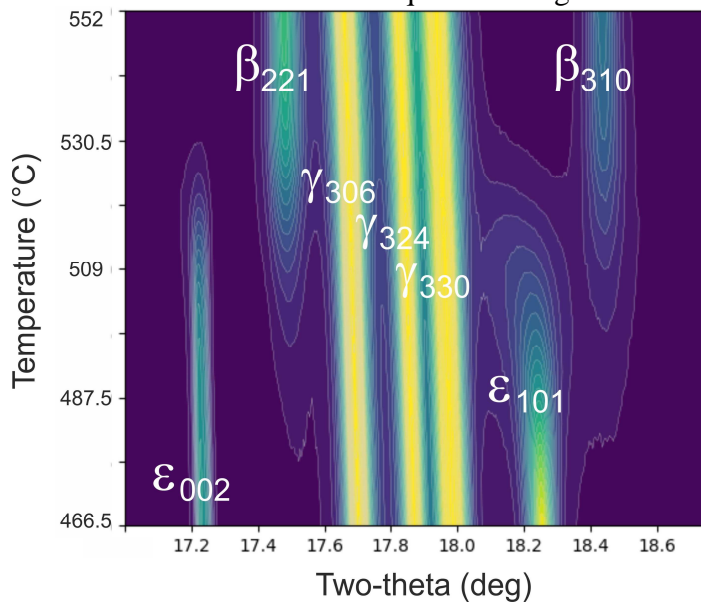


Fig. 3 Contour plot of the diffracted X-ray intensity for the ϵ to β -Mn phase transformation during heating.

Figure 3 shows the diffracted X-ray intensity recorded from X-ray spectra at various temperatures in the range of the ϵ to β -Mn phase transformation (466°C to 552°C). It can be observed that the phase transformation occurs abruptly, within a 20°C temperature range, however there is a small temperature range of about 5°C, centered at around 510-515°C where the two phases co-exist. The lines of the majority γ_2 phase have almost the same intensity throughout the whole investigated temperature range.

In conclusion, with respect to the 1st stage all the activities proposed in the work plane have been undertaken and the objectives have been attained. The results of the 1st stage, a stage that has been concluded in December 2017, have been categorized in agreement to the project objectives to be fulfilled in scientific, project management and dissemination. Scientific results, linked to and derived from the 1st stage activity related to the creation of MTJ elements, were mainly represented by the design of the free layer of the MTJ stack, the design of the MTJ multilayer structure. Project management results included the creation of the website, the risk management and the quality assurance plans as well as the annual report plan. The dissemination results have been concluded with communications at international conferences and 1 publication in ISI ranked journal.

Stage 2: Demonstration of light assisted magnetization reversal of the MTJ element. Conceptualization of the magneto-optic technology for integration onto Si substrate. (dec. 2018).

During the 2nd stage of the project, during 2018, the activities proposed in the work plan are related to development of MTJ elements for photonic assisted magnetization reversal and the realization of a magnetization switching of the free layer in MTJ with the help of a pulsed laser (photonic assisted switching mechanism). For this purpose, a MTJ structure made of multilayered heterostructures of Ta/ GdFeCo/Cu/[Pt-Co]/Ta have been prepared. The depositions have been made by rf and dc sputtering using the dedicated UHV sputtering facility described above. Rigorous control of the sputtering rates made possible the realization of the layered structure without significant intermixing of the sputtered elements, as proven by In situ observations and X-ray reflectivity studies. It has been recently proven by [R. John et al. Scientific Reports 7 (2017) 4114] that also FePt nanoparticles may exhibit magnetization reversal by femtosecond laser pulses, and also the reversal occurs through two different mechanisms: the helicity-dependent all-optical switching where the reversed magnetic orientation is defined by the optical angular momentum (or the helicity of the circularly polarized laser light), and thermally driven switching caused by laser heating with linearly polarized light. The second mechanism occurs mainly in the rare earth ferromagnetic compounds and has been explained through parallel alignment of the rare-earth and transition-metal sublattice magnetisations below the picosecond timescale. For this reason, layered systems containing both FePt or CoPt hard magnet layers and RE – containing layers such as GdFeCo are of interest for realization of our MTJ elements. Considering these issues, the choice of our heterostructure appears justified. The sample layout we prepared has the following deposition sequence: Glass substrate/Ta (3 nm)/[Pt(0.8 nm)/Co(0.7 nm)]5/Cu(8.1 nm)/Gd₂₀(FeCo)₈₀(5.6 nm)/Ta (3 nm). The individual GdFeCo and [Pt-Co] layers exhibit interlayer exchange coupling through the non-magnetic Cu layer, as obtained during the stage I of the project. The scheme of the layout model is provided in the Figure below. After performing the irradiation of the layout heterostructure with a 50 fs laser pulse we have measured the hysteresis loops and compared them with the ones measured before irradiations. The magnetic field has been applied perpendicular to the film surface. The magneto-optic Kerr effect usually measures the angle made by the K

vector (defined as the Kerr amplitude generated as a result of interaction of the light beam with the magnetization vector) with the normal plane of the film θ_K . The Kerr signal θ_K obtained for the MTJ heterostructure is presented in Figure 4. Normalized magneto-optic Kerr signal θ_K has been recorded as a function of the magnetic field that has been applied normal to the MTJ heterostructure plane. At very small negative fields we have recorded also minor loops (red and blue curves). These loops are showing no exchange bias behavior being centered on the $x = 0$ axis. These minor loops show sharp decrease of the magnetization from one spin state to another and accounts for the magnetization reversal of the free layer in the MTJ structure.

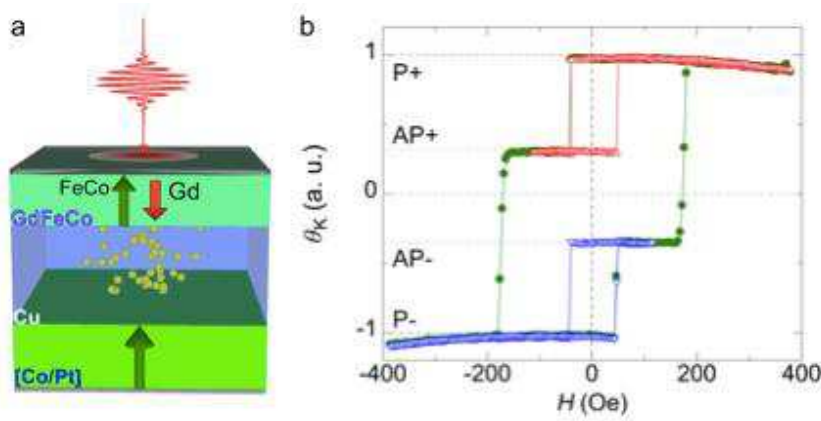


Fig. 4: Schematics of the MTJ structure made of Ta/ GdFeCo/Cu/[Pt-Co]/Ta. a) Sample layout of the model MTJ made of: Glass substrate/Ta (3 nm)/[Pt(0.8 nm)/Co(0.7 nm)]5/Cu(8.1 nm)/Gd20(FeCo)80(5.6 nm)/Ta (3 nm). The individual GdFeCo and [Pt-Co] layers exhibit interlayer exchange coupling through the non-magnetic Cu layer. Following laser irradiation on the GdFeCo side, high energy electrons are emitted by the surface of the free ferromagnetic layer, thus producing the magnetization switching of the [Co/Pt] magnetic layer. b) Kerr signal θ_K plotted as a function of the magnetic field (H) applied perpendicular to the film plane (minor loops proving the magnetization switching are shown in blue and red color).

The observed magnetization reversal mechanism is due to the electron flux determined by the irradiation with the laser pulse of the surface of the free ferromagnetic layer. These electrons hit the surface of the second ferromagnetic, hard magnetic, CoPt layer causing magnetization reversal in that layer. Magnetization vector of the two ferromagnetic layers may be reversed either parallel or antiparallel. The Kerr signal distinguishes clearly between four possible spin orientations. From the minor loops we estimated the magnetic exchange fields H_{BLEX} originating from the bilinear (ferromagnetic) coupling between the layers, as a function of interlayer distance. Two different coupling mechanisms excite the bilinear magnetic exchange fields: a magnetostatic interaction (so-called Néel or orange-peel coupling), with an exponential decay and a RKKY coupling (also known as quantum well coupling) where the decay is quadratic and oscillating as function of the interlayer thickness d_{Cu} :

$$H_{Ex}(d_{Cu}) = (H_0/d_{Cu}^2) \sin(\phi + 2\pi d_{Cu}/\lambda) + H_s e^{-d_{Cu}/t_s} \quad (1)$$

Here the first term is describing the RKKY coupling field and the second term the magnetostatic (or dipolar) coupling field. The constants H_0 , φ , λ corresponds respectively to the maximum exchange field, the phase shift and the oscillation period of the RKKY coupling and the constants H_s and t_s are respectively the dipolar field of the magnetostatic interaction and the thickness of the soft layer. Using equation (1) we fitted the bilinear exchange fields as function on the interlayer thickness. The results are displayed in fig. 5a and the estimated fit parameters are shown in Table 1.

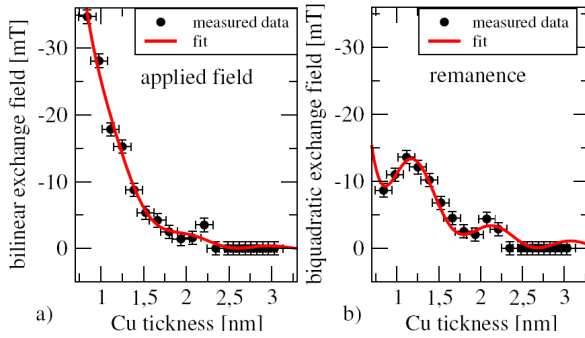


Fig. 4: Magnetic exchange fields as a function of interlayer thickness estimated from MOKE measurements with applied fields a) and in remanence mode b).

Parameter	H_{BLEX}	H_{BOEX}
H_0 [mT nm ²]	-2.2	-6.0
Φ	-0.4	-1.0
λ [nm]	0.91	0.91
H_d [mT]	-347	-69.5
T [nm ⁻¹]	0.37	0.61

Table 1: Calculated parameters as resulted from the fits using equation (1) with data shown in Fig. 5

We have also measured easy-axis minor loops in remanence mode, after temporarily applied magnetic fields. The areas of these minor loops are describing the biquadratic coupling energy $E_{BQ} = -J_2(m_1 \cdot m_2)^2$. However, the definition of the bilinear and biquadratic exchange fields is quite different, because of their asymmetric evolution. After the remanent coupling angles are induced to a maximum, only opposite applied fields are able to rotate the magnetisation vector back to a ferromagnetic alignment. There is no intrinsic reset force due to the biquadratic coupling. Nevertheless we used the definition for the bilinear exchange fields to estimate biquadratic exchange fields H_{BOEX} as function of the interlayer thickness, see Fig. 5b. We fitted these data using the same equation (1), the results of this fit being shown in Fig. 5. The parameters obtained from the fit are displayed in Table 1. One can see, that the influence of the oscillatory RKKY-coupling is more pronounced for the biquadratic exchange field than for the bilinear exchange field. Vlasko-Vlasov et al. have shown, that the field induced biquadratic coupling of a hard and soft magnetic layer can be described by an adaptation of the fluctuation model developed by Slonczewski. The assumption of this model is that the spatial coupling fluctuations are not caused by thickness variations of the nonmagnetic layer but by the spatial fluctuations of micromagnetic orientations of the hard magnetic layer. This leads to the same

biquadratic coupling behaviour as proposed in the model of Slonczewski. In this model, the magnitude of the BQ J_2 depends on the BL RKKY coupling J_1 , the size of the micromagnetic orientation (grain size) L , the intralayer exchange stiffness A_s and the layer thickness D .

$$J_2 = 4 \frac{(J_1)^2 L}{\pi^3 A_s} \coth\left(\pi \frac{D}{L}\right) \quad (2)$$

The remanent coupling angle between the magnetisation vectors can be calculated using the following formula: $\cos\theta_{rem} = (1-2f)J_1 / [2N(f)J_2 - K_s]$, where the function $N(f)$ is depending on the external fields and accounts, in first order, for the number of rotated micro magnetisations and thus changing effectively the coupling constants J_1 and J_2 . This mechanism results in a maximum of induced coupling angles, when the BL coupling constant J_1 is maximal.

In conclusion, the objectives foreseen for the 2nd year of the project development have been fully attained. Scientific results include the creation of MTJ elements for light assisted magnetization switching and the architectural design of the MTJ arrays with optical and electrical control. Due to the high potential of patenting our results, only a brief summary of our results may be publicly made available on the project webpage.

The 3rd year of the project development (2019) has been devoted to the conception and the design of a logic integration platform with magnetic element array. The activities for the 3rd year concerned: a) design of the process flux for creation of the integration platform b) integration of magnetic elements onto the dedicated platform.

a) *design of the process flux:*

The building block needed for the integration platform was made by using electron beam lithography and photo-lithography techniques. The aim of the processing procedure was to obtain nanostructures with specific shapes and geometries. We have performed, in this respect, a dose test using the electron beam lithography technique. For this purpose two photo-resist layers were applied on a Si(111) substrate with native SiO₂ protective layer grown on top. The first photo-resist layer applied was methyl methacrylate (MMA EL10) with a thickness of 400 nm. The second layer applied was poly-methyl methacrylate (PMMA A3) with a thickness of 100 nm. Each layer was deposited via spin-coating for 60 s, at a speed of 4000 rpm and acceleration of 500 rpm/s. After the deposition of each layer, the sample was heated at 175°C for 10 s in order to evaporate the solvent. Nanofabrication of the magnetic element considered in first instance Pt wires with various dimensions, ranging from 50 to 200 nm thickness and 7 µm length. The engraving of the wires was realized via electron beam lithography using a current of 11 pA. The size of the electron beam was 3 pixels, whereas the field magnification was 800x. It is known that in electron beam lithography, the resist performance in terms of exposure dose latitude, sensitivity, contrast, roughness and resolution, are influenced by the nature of the resist, the developer type and composition, and the development

technique. In our case the dose was incremented with 0.1 starting from 0.6 and ending at 0.79. The development was realized keeping the sample in a solution of methyl isobutyl ketone (MiBK) and isopropyl alcohol (IPA) (1:3) for 8 s and then in IPA for 1 min. Finally, the sample was dried with nitrogen gas flow. After the development, the reactive ion etching technique was implemented in order to have a better definition of the patterned shapes. A 10 s reactive ion etching process was realized in the dedicated UHV chamber at a pressure of 15 mbar. A layer of Pt with 30 nm thickness was deposited over the wire structure with an intermediate layer of Ti with 4 nm thickness. The deposition rate in the case of Pt was 0.25 nm/s, whereas the value corresponding to Ti deposition was 0.1 nm/s. The working pressure inside the deposition chamber was 10^{-7} mbar. The lift-off process was realized by placing the sample in acetone for 2 min at 50 °C and, afterwards, in acetone at room temperature for 30 min. Scanning Electron Microscopy (SEM) images of the wires were collected. Only the wires with an exposed thickness of 200 nm could be observed. The SEM image of wires having a real thickness of approximately 250 nm is presented in figure 1.

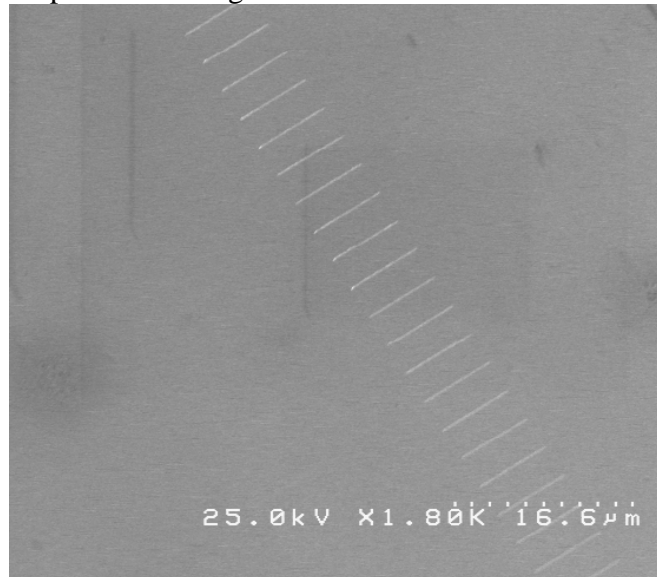


Figure 1. SEM image of wires with exposed thickness of 200 nm, obtained at different doses ranging from 0.6 (up) to 0.79 (down)

It was concluded that the appropriate dose for the wire engraving is 0.67. In order to obtain various types of structures (e.g. nanostructured circles and triangles) via electron beam lithography, two dose tests were performed. One test (test 1) differentiates from the other by the fact that reactive ion etching was implemented in order to improve the definition of the patterned shapes, while for the other case (test 2), the technique was not realized. The considered structures include: wires with 150 nm and 200 nm thicknesses, circles and equilateral triangles with a characteristic length of 200 nm, circles with diameter of 335 nm (tangent and overlapped on y direction over 200 nm) and equilateral triangles with characteristic length of 400 nm. The photo-resist application, the metal deposition and the lift-off procedures were similar to those presented in the case of the previous dose test.

For the two tests, the pattern was repeated at different values of the current: 17 pA, 10 pA and 15 pA. For each current value, different dose values were considered from 0.6 to 0.79, in steps of 0.1.

SEM images of the obtained structures can be seen in figure 2. We observed irregular shapes of the circles and triangles with exposed characteristic dimensions of 200 nm and 400 nm in the case of test 2. The area of the shapes were enlarged with almost 80 % with respect to the exposed area after performing reactive ion etching (test 1), but the shape of the structures remained relatively identical to the exposed shape. The best results obtained within test 1 were achieved for a current of 15 pA, the corresponding SEM images being shown in figures 2-4.

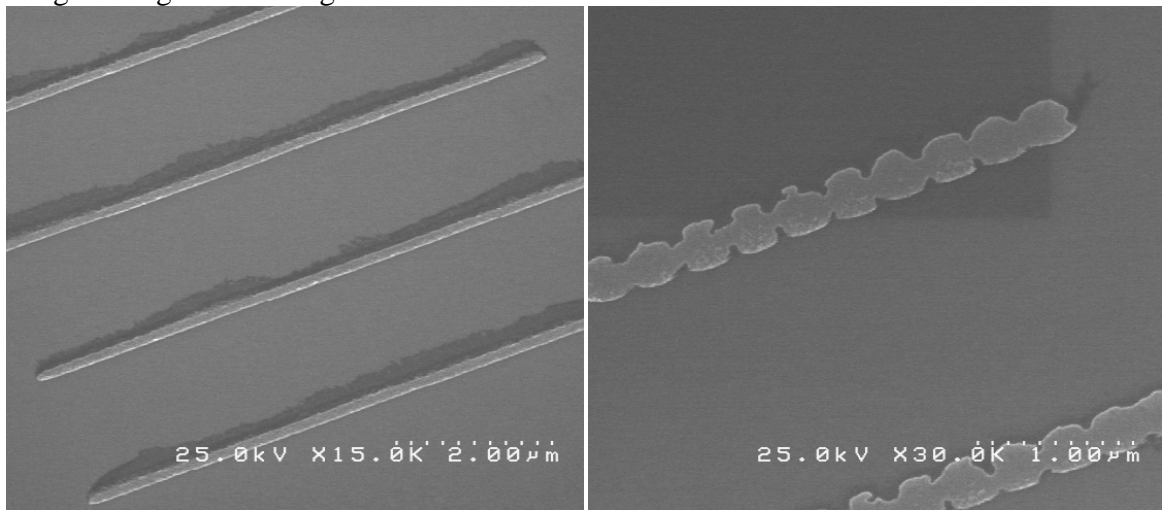


Figure 2. Wires with exposed thickness of 100 nm, each one corresponding to a dose in the interval 0.76-0.79 in ascending order from top to bottom (a) tangent circles with the exposed diameter of 200 nm at a dose of 0.75 (top) and of 0.76 (bottom) (b)

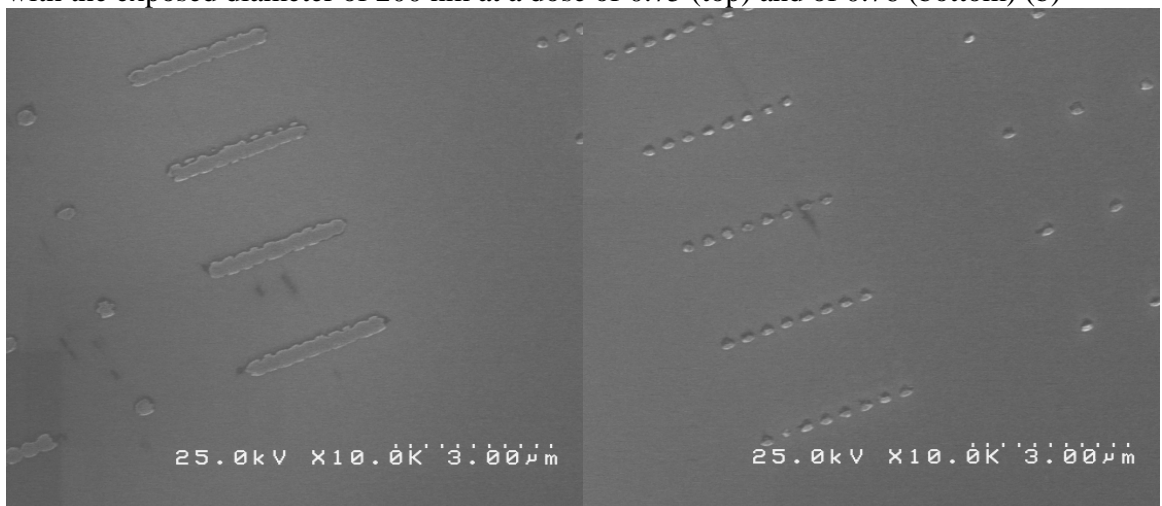


Figure 3. Circles with the exposed diameter of 335 nm and the same circles overlapped over a distance of 200 nm on y direction corresponding to a dose in the interval 0.76-0.79

in ascending order from top to bottom (a) circles with the exposed diameter of 200 nm spaced at a distance of 200 nm (left column) and at 1200 nm (right column) corresponding to a dose in the interval 0.75-0.79 in ascending order from top to bottom (b)

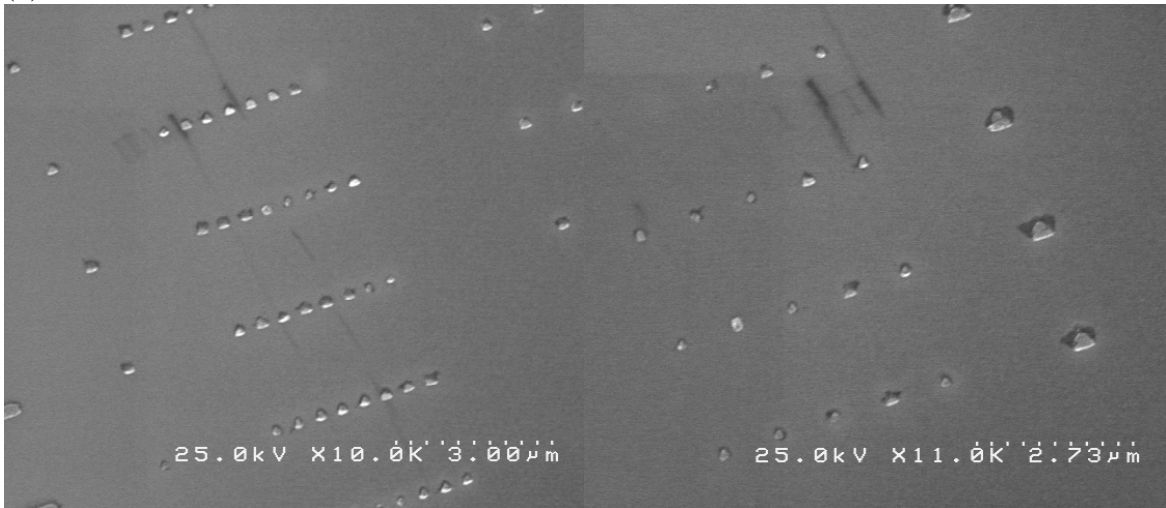


Figure 4. Equilateral triangles with exposed characteristic dimension of 200 nm spaced at a distance of 200 nm corresponding to a dose in the interval 0.77-0.79 in ascending order from top to bottom (a) equilateral triangles with exposed characteristic dimension of 1200 nm spaced at a distance of 200 nm corresponding to a dose in the interval 0.77-0.79 in ascending order from top to bottom (left column) and equilateral triangles with exposed characteristic dimension of 400 nm (right column) (b)

The best results obtained within test 2 were achieved for a current of 15 pA. The corresponding SEM images are shown in figures 5-7.

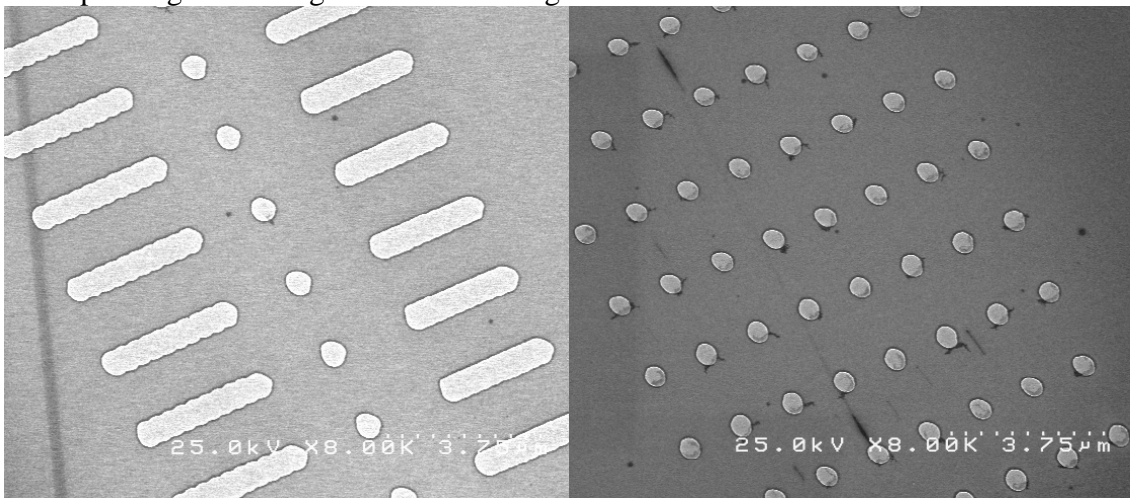


Figure 5. Tangent circles with the exposed diameter of 335 nm (first column); circles with exposed diameter of 335 nm (second column) circles with exposed diameter of 335 nm overlapped over 200 nm on y direction (third column) (a) circles with exposed diameter of 200 nm spaced at 1200 nm over x direction (b); the corresponding doses are in the interval 0.66-0.71 in ascending order from top to bottom.

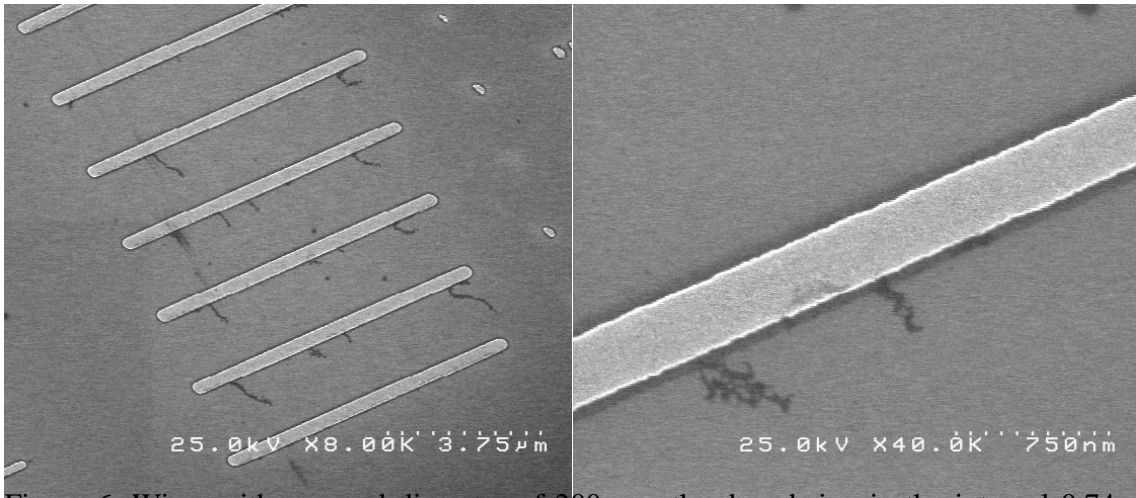


Figure 6. Wires with exposed diameter of 200 nm, the dose being in the interval 0.74-0.79 in ascending order from top to bottom (a) wire with exposed diameter of 200 nm, the corresponding dose being 0.78 (b)



Figure 7. Equilateral triangles with exposed characteristic dimension of 200 nm spaced over x direction at a distance of 1200 nm (second column), equilateral triangles with exposed characteristic dimension of 400 nm (third column)

We obtained various contacting patterns via photo-lithography using two different masks (see figure 8). We used a Si substrate covered with a 500 nm thick SiO₂ layer. S1805 resist was applied on the substrate via spin-coating. The wafer was spun for 10 s at a speed of 1000 rpm, afterwards it was spun for 30 s at a speed of 4000 rpm, and finally, it was spun for 2 s at a speed of 7000 rpm. The Si wafers were heated at 115 °C for 60 s after resist application. The UV exposure time was 20 s. The lift-off was realized keeping the wafers in MF-319 for 40 s. In the end, the wafers were cleaned with distilled water and dried with nitrogen.

Over the photo-lithography patterned contacting structures it was deposited an intermediate layer of Cr with 4 nm thickness and a 40 nm thick layer of Au via thermionic vacuum arc method. The base pressure was $4.2 \cdot 10^{-7}$ bar, whereas the working pressure was $4.2 \cdot 10^{-6}$ bar. The lift-off was realized keeping the samples in acetone at 50 °C for 4 min, then in ultrasonic bath for 4 s and, finally, in acetone at room temperature for 1 h.

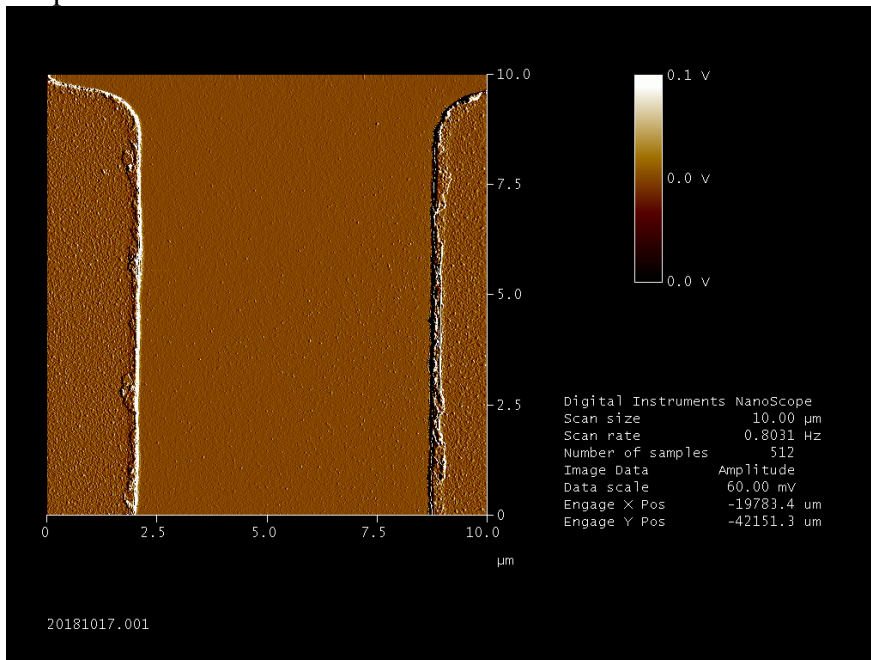


Figure 8. AFM image of a contacting region

The AFM image proved that the distance between contacts is 6.7 μm.

In this type of regions the following type of structures were engraved via electron beam lithography: tangent circles with the exposed diameter of 200 nm (i), circles with the exposed diameter of 200 nm spaced at 250 nm over x direction (ii) and identical circles spaced at 300 nm over x direction (iii).

The resist was removed keeping the sample in acetone at 50 °C for 2 min and in acetone at room temperature for 30 min.

After resist removal, a reactive ion etching treatment was carried with the same working parameters as described previously, excepting the decreased treatment time of 8 s.

b) integration of the magnetic element on the platform

The hybrid architectures have been subsequently obtained by deposition of the magnetic elements onto the logic conditioned prepatterned die. In order to achieve a regular and homogeneous dispersion, we have used a spin coater working in low vacuum (10^{-2} mbar) at 100 rpm. In the Fig. 8 the SEM images of the obtained hybrid structure with the nanoparticles deposited onto the logic conditioned device are shown. As we have used for deposition the supernatant nanoparticles solution, the concentration was quite low therefore the observed nanoparticles are organized mostly as traces along the conductive lines. It is worthwhile mentioning the tendency of the nanoparticles to organize at the edge of the conductive lines, the interface between the Si wafer substrate and the metallic line.

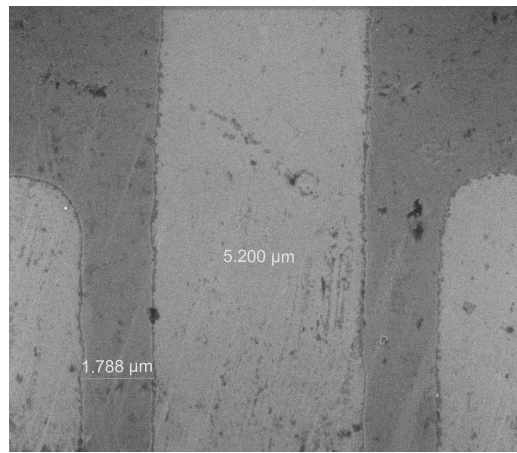


Fig. 8. Scanning electron microscopy images of the hybrid device obtained after deposition of NP solution onto the logic conditioned device (20000 x magnification)

The hybrid architectures have been subsequently obtained by deposition of the FeC nanoparticles. The Fe/FeC core-shell nanoparticles have been magnetically characterized using a Superconducting Quantum Interference Device SQUID facility in applied magnetic field of up to 5 T. Such device is highly sensitive, having a 10^{-6} emu resolution in the determination of the magnetic moment, allowing thus investigations on highly diluted magnetic systems and magnetic fluids. Nanoparticles solutions dispersed in CMC centrifugated for 1h and 5h and in chitosan centrifugated for 1h have been measured in special capillaries. Figs. 9 show the hysteresis loops of the FeC core-shell nanoparticles, loops recorded at 265K.

It can be seen that in the case of NP dispersed in CMC the behavior is of a soft magnetic material, which is typical for mono-phased materials based on Fe. Magnetization rises sharply and reaches saturation at very low applied fields. From the graphs we have determined that the saturation fields are 794, 639 and 568 kA/m, respectively for the loops from Figures 9a, b and c, meaning higher than the magnetic field necessary to surmount the shape anisotropy of the spherical Fe nanoparticles. The situation is similar for the two CMC dispersed NP solutions. It can be seen that the saturation field is slightly lowered for the NPs in CMC centrifugated for 5h as well as in

the case of NPs in other carrier. This implies an apparent process of softening of the magnetic character mainly due to the nanograins slight structural refining during higher centrifugation times for the NPs in CMC. The saturation magnetization is quite close for the two samples: 73 emu/g for the sample centrifugated for 1h and 69 emu/g for the sample centrifugated for 5h. We have estimated also the remanence-to-saturation magnetization ratio and found it to be 0.31, 0.42 and 0.67 respectively for Figures 9a, b and c however due to the limited number of experimental points near zero applied field the first two values are to be taken cautiously, since also the coercive field in the two cases of NPs dispersed in CMC is extremely low (23 and 31 kA/m respectively).

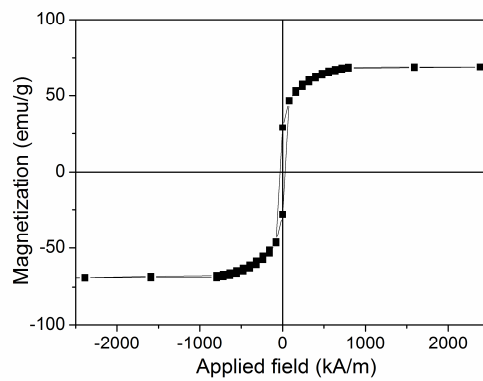


Fig. 9a: 265K Hysteresis loop of NP's dispersed in CMC centrifugated for 1h.

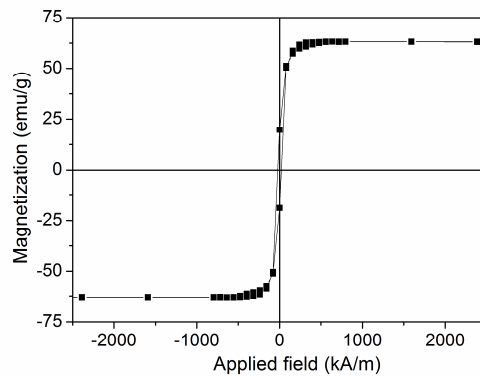


Fig. 9b: 265K Hysteresis loop of NP's dispersed in CMC centrifugated for 5h.

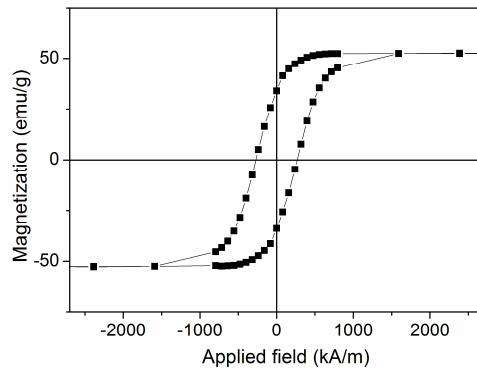


Fig. 9c: 265K Hysteresis loop of NP's dispersed and centrifugated for 1h. $H_c = 270$ kA/m

A different situation is encountered though for the Fe/FeC NP dispersed. A clear increase of the coercivity (about 270 kA/m) is observed for this sample (Fig. 9c) compared to the other ones. This increase of coercivity may signal the occurrence of pinning fields and spin freezing in magnetic configurations with linear domain walls. Due to that fact, during centrifugation a fraction of NPs can become agglomerated and increase the magnetic coherence volume. This fraction of NPs would have increased mean size and higher exchange correlation lengths, and consequently would lead to an increased coercivity. It may eventually facilitate the detection of a high magnetoresistive signal, due to the spin-dependent electron transport along the conductive current lines – the logic conditioning – through the magnetic nanoparticles deposited onto these lines. In the case of a spin frozen magnetic configuration, this spin-dependent signal will be in phase and easier to detect in normal four-point-probe measurement configuration of the GMR.

As mentioned before, the hybrid structure has been obtained by deposition of highly diluted NP solutions onto the prepatterned, logic conditioned, interdigitated die. The unit consists of repeated independent logic structures of 4 x 4 mm onto a total area of 8 x 16 mm. The conductive lines are in such way configured / preconditioned as to allow either a four-point-probe measurement protocol (4 pads) or a two-point-probe protocol (2 pads, see Figs. 1, 2). In order to obtain the magnetic features of the whole hybrid structure, we have performed magnetization measurements using SQUID magnetometry at 300K. The resulting hysteresis loop of the hybrid structure is shown in Figure 10.

A similar hysteresis loop as in the case of as-synthesized nanoparticles is obtained. A saturation magnetization of the measured area of the device of about 44 emu/cm^2 has been obtained with a net magnetic moment of the diluted NP of about $2.5 \times 10^{-3} \text{ emu}$. As the density of the deposited magnetic nanoparticles is well below 1 monolayer of nanoparticles, this quite high value of saturation magnetization is very promising and shows potential for obtaining magnetoresistive signal and good perspectives in view of potential applications in spintronics.

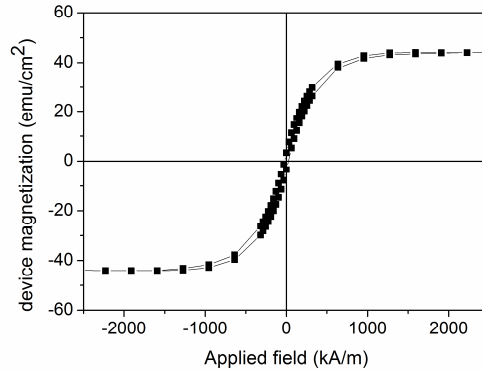


Fig. 10: 300K Hysteresis loop of hybrid device obtained by deposition of NP's dispersed in chitosan onto the logic conditioned interdigitated die.

3.4. Magnetotransport behavior of the hybrid structure

Magnetoresistive measurements have been performed on the surface of the hybrid structure using a Physical Property Measurement System PPMS 5 in four-point-probe setup. The facility allows measurements from 1.2 K up to 300K in an applied field of up to 5.5 T. We have chosen two different measurement geometries: the conductivity in-plane (CIP) using only two pads and the cross-over geometry, using all 4 pads. For the cross-over configuration, we have chosen the unit having the layout 2, with 4, 300 microns wide, pads, and 1.5 microns wide conductive lines. Layout 1 with two pads was used for measuring the magnetoresistance in CIP geometry. Both measurements have shown variations of the resistivity with the applied field, thus proving that such hybrid structure may be effective in applications as magnetic sensors.

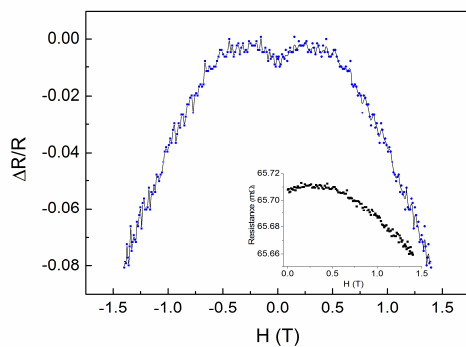


Fig. 11a: GMR response of the hybrid structure in positive and negative applied field at 4.2 K, in CIP configuration. Inset: the absolute magneto-resistance vs. applied field (positive branch)

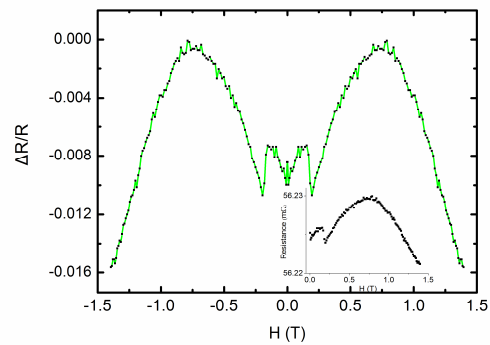


Fig. 11b: GMR response of the hybrid structure in positive and negative applied field at 4.2 K, in cross-over configuration. Inset: the absolute magneto-resistance vs. applied field (positive branch)

Figs. 11 show the magnetoresistive curves as a function of the applied field, recorded at 4.2 K, in CIP and cross-over configuration, respectively. The magnetoresistance is given by the $\Delta R/R$ ratio defined as:

$$\frac{\Delta R}{R}(T, H) = \frac{R(T, H) - R(0)}{R(0)} \quad (1)$$

where $R(T, H)$ is the resistance at a given H of the applied field and at a given temperature T and $R(0)$ is the resistance at the temperature T in the absence of the applied field. In the inset we have shown also the absolute magneto-resistance vs. applied field (positive branch). It is seen that the magneto-resistance ranges between 53-65 m Ω , values that are consistent with those obtained in other diluted nanoparticles systems and spin valves.

It can be seen for both configurations the symmetry of $\Delta R/R$ branches when the applied field is positive or negative. There is no hysteresis of the magnetoresistance. In both cases the GMR response is not saturated at 1.5 T, being thus possible to obtain an even higher GMR response if the applied field is increased. In the CIP configuration the hybrid structure shows the highest GMR, of about 8% at 4.2 K. It is a significantly high GMR value that may allow the use of such hybrid structures as magnetic GMR sensors. In the cross-over configuration the GMR effect recorded is only 1.6% at 4.2 K, due mainly to the purely resistive component of the electron transport. It is widely known that the GMR effect is given by the spin dependent scattering of the conduction electron at the magnetic / conductive interface. But a non-negligible component is given also by the scattering inside the magnetic nanograins. It appears that a higher number of conductive / magnetic interfaces correlated to lowered nanograin sizes is an essential conditions to minimize the intra-particulate scattering and consequently to improve the GMR response.

In conclusion, the objectives foreseen for the 3rd year of the project development have been fully attained. Scientific results included the design of the flux process for creation of a logic conditioned platform as well as the integration of magnetic elements on the platform, realization of a hybrid device and detecting of the giant magnetoresistance signal from the device, an essential step in view of further exploitation in spintronic devices. Due to the high potential of patenting our results, only a brief summary of our results may be publicly made available on the project webpage.